Acta Materialia 240 (2022) 118315

Contents lists available at ScienceDirect

Acta Materialia

journal homepage: www.elsevier.com/locate/actamat

Full length article

Tensile and compressive stresses in Cu/W multilayers: Correlation with microstructure, thermal stability, and thermal conductivity

Giacomo Lorenzin[a,1], Md Shafkat Bin Hoque[b,1], Daniel Ariosa[e], Lars P.H. Jeurgens[a], Eric R. Hoglund[c], John A. Tomko[b], Patrick E. Hopkins[b,c,d], Claudia Cancellieri[a,*]

[a] Empa, Swiss Federal Laboratories for Materials Science and Technology, Laboratory for Joining Technologies and Corrosion, Ueberlandstrasse 129, 8600 Duebendorf, Switzerland
[b] Department of Mechanical and Aerospace Engineering, University of Virginia, Charlottesville, VA 22904, USA
[c] Department of Materials Science and Engineering, University of Virginia, Charlottesville, VA 22904, USA
[d] Department of Physics, University of Virginia, Charlottesville, VA 22904, USA
[e] Instituto de Física, Facultad de Ingeniería, Universidad de la República, Herrera y Reissig 565, C.C. 30, Montevideo 11000, Uruguay

ARTICLE INFO

Article history:
Received 23 May 2022
Revised 5 August 2022
Accepted 28 August 2022
Available online 30 August 2022

Keywords:
Nanomultilayers
Internal stress
Microstructure
Thermal conductivity

ABSTRACT

The internal stress and microstructure in nanomultilayers strongly affect their reliability and performance, especially towards higher service temperatures. The initial stress and microstructure can be controlled during the growth by opportunely changing the deposition parameters. The intrinsic stress state can be tuned to achieve stress states ranging from compressive to tensile. In the present work, Cu/W nanomultilayers with opposite stress states (tensile and compressive) were fabricated by magnetron sputtering. The stress is found to be strongly correlated to the microstructure and internal disorder, as measured by X-ray diffraction and photoemission. In particular, higher disorder at the internal interfaces occurs in the presence of tensile growth stresses. The compressive nanomultilayers exhibit a more ordered structure, which improves their thermal stability up to 800 °C. The different microstructures for the opposite stress states significantly impact the thermal stability and thermal conductivity of the nanomultilayer stack. Our study thus sheds light on the correlations between the stress state, microstructure, thermal stability and thermal conductivity of Cu/W nanomultilayers.

1. Introduction

Nanomultilayers (NMLs) are commonly formed by alternatively stacking nanolayers of a metal or an alloy and a chemically inert barrier (e.g., oxides, nitrides or refractory materials). They are an important and innovative solution for low temperature joining technologies [1], in particular for brazing [2–4]. The interest in NMLs resides also in their capability of serving as interconnects in microelectronics [5–10], optical coatings [11,12], semiconductor devices [13], radiation-tolerant coatings [14], heat armors, and sinks in plasma experiments [15]. Among different types of NMLs, Cu/W multilayers are particularly suitable for these applications because of their longstanding reliability, durability, and scalability [10,13,14,16–18].

Magnetron sputtering, a type of physical vapor deposition (PVD), is a widespread method to produce thin films and nanomultilayers (NMLs) with targeted composition, thickness, and roughness. In general, multilayers produced by magnetron sputtering bear a stress, generated during the film growth, and hence denominated “growth stress” or “intrinsic stress”. It represents an important property of thin films because it can lead to their failure, therefore affecting their durability and reliability. For this reason, intrinsic stress in sputtered single-material thin films has been deeply investigated in past decades [19–22]. There is a widespread agreement in classifying the materials behavior in two categories [23,24]. To the first category belong Type I materials, such as W, Ta, Cr and Fe. They have low atomic mobility and high melting temperature and are prone to generate tensile stress during growth. To the second category belong Type II materials, such as Cu, Al, Ag and Au. These materials possess high atomic mobility and low melting temperature and are characterized by a compressive-stress generation during growth. However, sputtering deposition parameters can influence the stress-generation mechanisms and play a

* Corresponding author.
E-mail address: claudia.cancellieri@empa.ch (C. Cancellieri).
[1] Giacomo Lorenzin and Md Shafkat Bin Hoque contributed equally to this work.

https://doi.org/10.1016/j.actamat.2022.118315

Table 1
Deposition parameters used to grow the tensile and compressive NMLs.

	Ar-pressure (Pa)	Gun power (W)
Tensile NML	2	80
Compressive NML	0.267	100

crucial role in determining the overall stress state. Type I materials displaying a tensile stress and Type II materials with a compressive stress have been well documented. Therefore, the correlation between sputtering deposition parameters and thin films microstructure and stress state has been well studied [25–30]. An analogous study on intrinsic stress has not been performed as extensively for NML systems. A few studies focusing on this topic include the pioneering works of Spaepen et al. [31,32] and Clemens et al. [33]. However, the stress evolution in a multilayer structure was not related to specific properties. Therefore, the microstructure-stress-properties relationships in NML systems still remain largely unadressed in the literature. In this study, Cu/W multilayers with opposite stress states, highly tensile and compressive, were successfully fabricated. The connection of the tensile and compressive stresses with the microstructure and thermal conductivity is presented in relation to the thermal stability by combining different characterization techniques. Our results reveal that the tensile multilayers display higher disorder at the interfaces with respect to the compressive one. As shown in the present work, the thermal stability and thermal conductivity are strongly affected by the stress state and microstucture of the NML. The thermal conductivity of the compressive sample is almost 2.5 times higher compared to the tensile specimen. Additionally, the thermal conductivity of the compressive and tensile specimens exhibits completely different trends as a function of annealing temperature.

The multiple characterizations performed in this work reveal the effects of different fabrication, processing and thermal loading conditions on the stress, microstructure and properties of Cu/W nanomultilayers. The obtained results can be used to predict the role of microstructure and stress on properties of other NMLs combining Type I and Type II materials as well as other immiscible systems, such as Cu/Mo, Ag/Cu, Cu/Cr, Cu/Nb, and Ag/W. In addition, this work offers an example of how to produce nanocomposite (NC) coatings with tailored properties. In fact, annealing treatments transform NMLs into NCs, whose properties depend on parent NMLs stress and microstructure, which can be tuned by adequately selecting sputtering deposition parameters. Also the NML-to-NC transition temperature is related to the parent NML properties and, hence, can be controlled.

2. Experimental

2.1. Sample preparation

The Cu/W nanomultilayers (NMLs) were grown by DC magnetron sputtering in an ultra-high vacuum (UHV) chamber with base pressure of $< 5 \times 10^{-9}$ mbar. The multilayers were grown on Si(001) substrates that have 90 nm of amorphous $a-Si_3N_4$ on top. This $a-Si_3N_4$ layer prevents interdiffusion between the Si substrate and the Cu/W NML during the high-temperature annealing, which could result in the unwanted formation of Si-Cu intermetallics. Prior to the deposition, an RF bias of 100 V at 1.6×10^{-2} mbar was applied for 2 min to remove residual surface contaminants after ultrasonic cleaning in acetone, ethanol and isopropanol. 10 nm of Cu and 10 nm of W repeated 10 times were grown on a 25 nm W layer working as buffer. The chosen deposition parameters are reported in Table 1 in Section 3.1.1. Their optimization to tune the stress to compressive and tensile values is described in Ref. [34]. After the deposition, selected samples underwent an isothermal annealing process for 100 min at 300 °C, 600 °C, 800 °C, or 850 °C in high vacuum (pressure $< 10^{-5}$ mbar) with a heating ramp of 20 K/min in a CVE (Cambridge Vacuum Engineering) HL 1218 oven.

2.2. Characterization techniques

2.2.1. Multi-beam optical stress sensor

The sputter deposition chamber is equipped with a Multi-beam Optical Stress Sensor (MOSS) system (k-space Associates) for in-situ measurement of the substrate curvature during thin-film and multilayer growth (see Fig. S1 in the Supplementary material) [35,36]. In this setup, a 3x3 array of laser beams hits and is reflected back from the substrate surface under a (near-)normal incidence angle. The real time evolution of the substrate curvature was calculated from the change in the average spacing between adjacent laser spots in the array, with a typical curvature resolution of about 3×10^4 m^{-1}. From the curvature, $1/\rho$, stress-thickness values, $\sigma \cdot h$, i.e., the product between the average stress and film thickness, can be derived according to the well-known Stone's equation [37,38]:

$$\sigma \cdot h = \frac{M_s h_s^2}{6} \frac{1}{\rho} \tag{1}$$

where M_s is the substrate bulk modulus (180.5 GPa for Si) and h_s is the substrate thickness (200 μm). Information on average stress and incremental stress in the sample can be derived, respectively, by dividing $\sigma \cdot h$ by the film thickness, $\sigma = \frac{\sigma \cdot h}{h}$, or with a derivative operation, $\sigma_i = \frac{d(\sigma \cdot h)}{dh}$.

2.2.2. X-ray diffraction

A Bruker D8 Discover X-ray diffractometer operating in Bragg-Brentano geometry with Cu K_α radiation at 40 kV/40 mA was used to measure the Bragg–Brentano $\theta - 2\theta$ scans, the mean residual stress, and the pole figures for texture analysis. Stress analysis was carried out in point focus geometry, at room temperature, using the Crystallite Group Method (CGM) [39,40], suitable for highly textured systems (deposited Cu/W NMLs possess a pronounced out-of-plane Cu{111} ‖ W{110} texture [17,41]). Multiple reflections belonging to the Cu{11 − 2} and W{1 − 21} crystallite groups were selected for stress analysis [42]. All annealed NMLs were measured ex-situ after cooling down to room temperature (RT).

2.2.3. X-ray photoelectron spectroscopy

The chemical composition of NMLs was evaluated by X-ray photoelectron spectroscopy (XPS) using a PHI Quantes spectrometer (ULVAC-PHI) equipped with a conventional low-energy Al-K_α X-ray source (1486.6 eV) and a high energy Cr-K_α (5414.7 eV) X-ray source. The energy scale of the hemispherical analyzer was calibrated according to ISO 15472 by referencing the Au $4f_{7/2}$ and Cu $2p_{3/2}$ main peaks (as measured in-situ for corresponding sputter-cleaned, high-purity metal references) to the recommended binding energy (BE) positions of 83.96 eV and 932.62 eV, respectively. Notably, the XPS instrument is directly connected to the sputter chamber, thus allowing in-situ sample transfer after the deposition under UHV conditions (see Fig. S2 in the Supplementary material). In this way, air-exposure prior to surface analysis of as-deposited samples could be prevented. Survey scans were acquired with a pass energy of 280 eV and a step size of 0.5 eV. Detailed scans of the Cu 2p, W 4d, O 1s, C 1s, N 1s and W 4p regions for the as-deposited (not air-exposed) and annealed (air-exposed as a consequence of the ex-situ annealing step) were measured with a step size of 0.2 eV and a pass energy of 112 eV. The atomic concentrations were calculated from the peak areas after Shirley background subtraction using the predefined sensitivity factors in the MultiPak

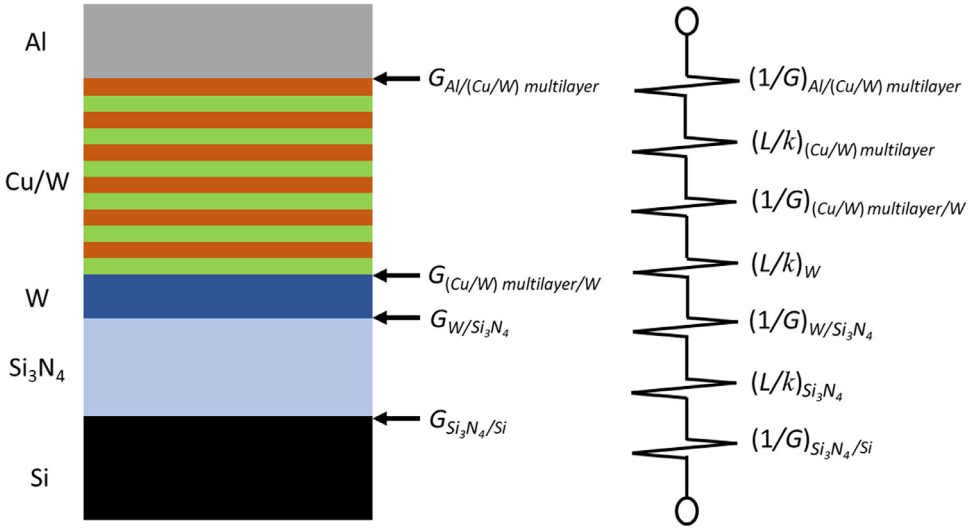

Fig. 1. Schematic diagram of the sample geometry exhibiting the thermal resistances between the Al film and Si substrate.

9.9 software provided by ULVAC-PHI. Compositional depth profiles were acquired by alternating cycles of XPS analysis ($Al-K_\alpha$, 51 W, 200 μm beam diameter) and sputtering with a focussed 1 kV Ar^+ beam rastering a 2×2 mm^2 area.

2.2.4. SEM and STEM

Focused Ion Beam (FIB) cuts were performed and cross section images were acquired in an FEI Helios NanoLab 660 Dual-Beam Scanning Electron Microscopy (SEM) and FIB system. The FIBing process was done with a focussed Ga^+-ion beam at an acceleration voltage of 30 kV. Successive cutting steps at decreasing ion currents (9.3 nA, 0.79 nA, and 0.23 nA) were performed to polish the cut surface. Cross-sectional SEM analysis was performed at an acceleration voltage of 2 kV in Backscattered Electrons (BSE) mode. The surfaces of the samples (as deposited and annealed) were imaged with an Hitachi S-4800 field emission gun SEM using an acceleration voltage of 2 kV and with the detector in the Secondary Electrons (SE) mode.

Scanning transmission electron microscopy (STEM) was performed on a Thermo Fisher Scientific Themis Z-STEM equipped with a Super-X energy dispersive X-ray (EDS) detector operating at 200 kV with a 30 mrad, 400 pA probe. Medium angle annular dark field images were acquired during EDS acquisition, which provide diffraction contrast. Cross-section samples for STEM were prepared using a Thermo Fisher Scientific Helios Dual-beam Focused Ion-beam. Initial milling was performed at 30 kV and the final cleaning was performed at 5 kV.

2.2.5. Optical pump-probe techniques: time-domain thermoreflectance and steady-state thermoreflectance

Optical pump-probe technique time-domain thermoreflectance (TDTR) [43–46] was applied to investigate the effects of the intrinsic stress state and annealing temperature on the cross-plane thermal conductivity of Cu/W NMLs. Details of the applied two-tint TDTR setup are provided elsewhere [47–49]. Prior to the TDTR measurements, an ~80 nm aluminum (Al) film was deposited atop the sample surface via electron beam evaporation, which serves to convert the optical energy of the laser into thermal energy. A schematic diagram of the entire sample geometry is presented in Fig. 1. A total of seven resistances between the Al transducer and Si substrate were implemented for the TDTR data analysis. TDTR can measure the top two resistances as long as the other five are known. To determine the thermal resistance of the Si_3N_4 layer, we measured the thermal conductivity of a ~90 nm Si_3N_4 film via TDTR. The thermal resistance of the ~25 nm W layer was adopted from literature [13,50,51]. Furthermore, we assumed that the intrinsic thermal resistances of the Cu/W NML, W, and Si_3N_4 layers are significantly higher than the associated interfacial resistances [13,52]. Consequently, the interfacial resistances were disregarded. Additional details regarding the parameters used in TDTR analyses can be found in our previous publication [13].

To validate the assumptions used for the TDTR measurements and analysis, we employed another pump-probe technique named steady-state thermoreflectance (SSTR) [53–56]. Details of the SSTR setup and measurement procedures are provided in Braun et al. [53] and Hoque et al. [54]. The thermal penetration depth of the SSTR technique is significantly higher compared to TDTR [55]. Therefore, using large $1/e^2$ pump and probe radii (~20 μm), we fitted the seven resistances between the Al transducer and Si substrate as a single interfacial resistance in SSTR. This single interfacial resistance (Rth) can be expressed by the following equation:

$$R_{th} = \left(\frac{1}{G}\right)_{Al/(Cu/W)multilayer} + \left(\frac{L}{\kappa}\right)_{(Cu/W)multilayer} + \left(\frac{1}{G}\right)_{(Cu/W)multilayer/W} + \left(\frac{L}{\kappa}\right)_{W} + \left(\frac{1}{G}\right)_{W/Si_{3N_4}} + \left(\frac{L}{\kappa}\right)_{Si_{3N_4}} + \left(\frac{1}{G}\right)_{Si_{3N_4/Si}} \quad (2)$$

where L, κ, and G are layer thickness, thermal conductivity and thermal boundary conductance, respectively (the subscripts are self-explicative).

3. Results and discussion

3.1. As-deposited Cu/W NMLs

3.1.1. Microstructure and stress state

As demonstrated in Ref. [34], both a high Ar-pressure and a low gun power favor the generation of tensile stress during the growth of Cu and W single layers by magnetron sputtering. Vice versa, a low Ar-pressure and a high gun power were correlated with compressive growth stresses in Cu and W single layers. Analogous trends are reported in the literature both for Cu [57–59] and for W [60,61]. Based on these findings for Cu and W single-layer growth, the deposition parameters in the present study could be selected such to produce Cu/W nanomultilayers (NMLs) with an

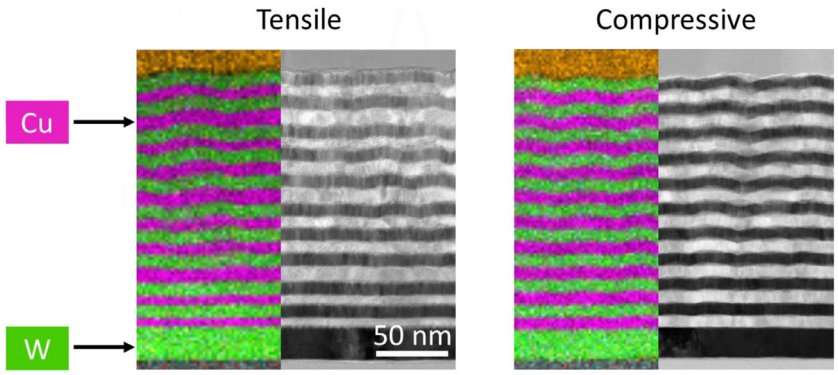

Fig. 2. Cross-sectional MAADF-STEM images of the tensile and compressive nanomultilayers (greyscale) showing diffraction contrast and overlaid EDS elemental mapping of Cu and W (colors).

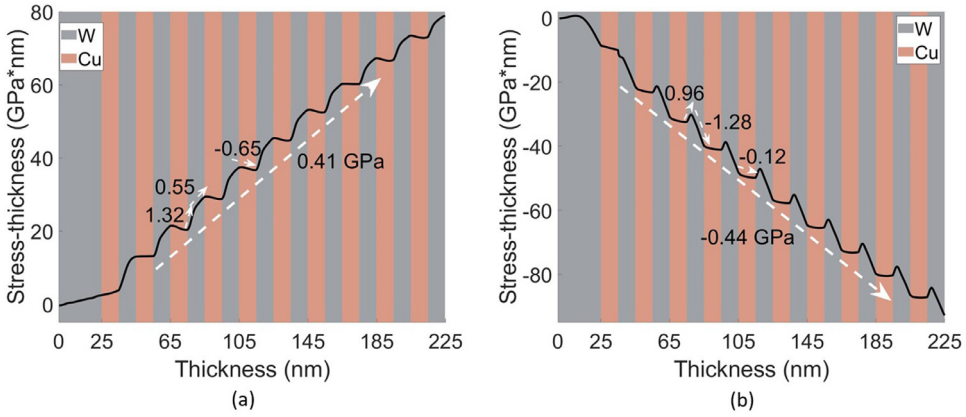

Fig. 3. Stress-thickness curves of (a) a tensile NML deposition run and (b) a compressive NML deposition run, as monitored in-situ with the MOSS (Section 2.2.1).

overall (i.e., on average) compressive and tensile state. The corresponding deposition parameters for the compressive and tensile Cu/W NML are reported in Table 1.

The microstuctures of the as-deposited compressive and tensile NMLs were investigated by cross-sectional STEM. Fig. 2 shows cross-sectional STEM images of the tensile and compressive NML overlaid with the corresponding EDS maps. The Cu and W nanolayers are straight and planar in the bottom of the NML stacks, but roughen towards the NML surface. The individual W layer thicknesses are rather constant and very similar for the compressive and tensile NML stacks. On the contrary, the thicknesses of the individual Cu layers appear less homogeneous and less constant throughout the stack for the tensile NML (even thought the deposition rates for both NMLs were carefully calibrated using single-layer deposition runs). The constrast in the MAADF-STEM images indicates that the tensile NML has a smaller grain size as compared to the compressive NML, which is consistent with the SEM characterizations (see below).

The stress evolutions during the tensile and compressive NML deposition runs were monitored in-situ with the MOSS (Section 2.2.1). Fig.s 3 a and 3 b display stress-thickness data acquired during the deposition of tensile and compressive NMLs, respectively. According to the stress-thickness data, Cu/W NMLs follow the same relationship between growth conditions and stress state as Cu and W single films. This is not obvious *a priori* because it has been reported that these two immiscible materials display different stress evolutions when grown as a single layer or as a combined bilayer in a NML structure, depending on the parent substrate [34]. The same "deposition parameters - stress state" relationship in sputter-grown Cu/W NMLs, particularly in correlation with the Ar-pressure, has been reported also in another recent work [62].

As determined by the interfacial energies in play, W and Cu grow according to the Volmer-Weber (VW) growth mode, characterized by three stages: islands nucleate on the underlying layer (pre-coalescence stage); islands grow and zip together (coalescence stage); the film continues its growth (post-coalescence stage) [63]. It is possible to associate every stage of the VW growth mode to specific features in stress-thickness curves. In general, compressive stress is generated during the pre-coalescence stage, tensile stress during the coalescence stage, and compressive or tensile in the post-coalescence stage based on adatom energies [24,34,64]. We can recognize some of these stages also in the stress-thickness data in Fig. 3a and b.

For the tensile NML, each successively deposited W layer develops a tensile stress: initially the corresponding incremental stress is 1.32 GPa, but this values decreases to 0.55 GPa from approximately half of the deposition step until the end. This stress evolution is consistent with the coalescence and post-coalescence stages of Type I materials (see Introduction). Each successive Cu deposition step during the tensile NML deposition run is associated with a constant negative incremental stress of −0.65 GPa.

For the compressive NML, each successively deposited W layer exhibits an initial tensile stage (with an incremental stress of 0.96 GPa) which is reversed into a compressive stage (with an incremental stress of −1.28 GPa). Once more, this behavior is in agreement with that of Type I materials grown at low Ar-pressures and high applied powers [65]. Similarly to the tensile NML, each successive Cu deposition step layer is associated with a slightly negative and approximately constant incremental stress of −0.12 GPa.

In both deposition runs, it appears that each W deposition step is associated with grain coalescence and layer growth on Cu, as evidenced from the recurrence of a coalescence and a post-coalescence stage. Strikingly, a pre-coalescence stage is neither observed for the tensile nor for the compressive NML. This happens because new W islands nucleate on the grains of the underlying polycrystalline Cu layer and directly interact and hold together with them. As a consequence, tensile stress is introduced from the onset of each W deposition step, thus skipping the first compressive stage associated with isolated island growth [32,66]. The Cu deposition steps exhibit a peculiar behavior for both the tensile and compressive NML depositions: i.e., neither pre-coalescence nor coalescence features are observed at the beginning of each Cu deposition step. Nonetheless, we cannot conclude that Cu changes its growth mode. In fact, pre-coalescence and coalescence stages for the Cu depositon steps might occur too rapidly to be detected (as also postulated in Ref. [34]). STEM analysis in Fig. 2 confirms layer formation during each Cu deposition step.

At the end of the deposition tensile and compressive runs, the average stress values derived from substrate curvature (SC) are $\sigma_{\mathrm{SC,\ tens}} = (0.403 \pm 0.007)$ GPa and $\sigma_{\mathrm{SC,\ compr}} = (-0.441 \pm 0.005)$ GPa, respectively. These values can be compared to the residual stresses of Cu and W in the as-deposited NMLs, as measured by ex-situ XRD (see Section 2.2.2): i.e. $\sigma^{\mathrm{Cu}}_{\mathrm{XRD,\ tens}} = (0.66 \pm 0.03)$ GPa and $\sigma^{\mathrm{W}}_{\mathrm{XRD,\ tens}} = (1.5 \pm 0.1)$ GPa for the tensile NML and $\sigma^{\mathrm{Cu}}_{\mathrm{XRD,\ compr}} = (-1.8 \pm 0.4)$ GPa and $\sigma^{\mathrm{W}}_{\mathrm{XRD,\ compr}} = (-3.84 \pm 0.09)$ GPa for the compressive NML. The sign of the average stress values in the as-deposited NMLs, as determined independently by XRD and MOSS, are consistent, although their magnitudes is different (i.e., XRD indicates higher average stress levels). Indeed, XRD estimates the average stress in the individual crystalline phase(s) [67], whereas the substrate curvature method estimates the average stress due to various sources, such as crystalline phases (as XRD), non-crystalline regions as well as interfaces (e.g., phase and grain boundaries) [40].

3.1.2. Texture and structural disorder by XRD

The in-plane and out-of-plane textures of the as-deposited tensile and compressive Cu/W NML are reflected by pole figures of Cu{111} and W{110} families of planes in Fig. S3 in the Supplementary material. The pole figure of the compressive NML shows a very clear, well-defined ring at 70.5° tilt angle for Cu{111}, and at 60° for W{110} (Fig. S3c and Fig. S3d), as expected for Cu{111} and W{110} fiber textures (with a well-defined out-of-plane and a random in-plane orientation of the respective grains). The tensile sample, on the other hand, has a broader ring for both reflections (Fig. S3a and Fig. S3b). This indicates a broader spread of crystal orientations for the tensile specimen, despite the fact that it is still strongly textured along Cu{111} and W{110}. This results in a higher polar angular disorder, and hence a more disordered structure. The standard $\theta/2\theta$ measurements confirm the aforementioned results. They were analyzed using a model calculation to reproduce the diffraction patterns, introduced in Ref. [41]. It uses a kinematic formalism and relies on two types of disorder of different nature:

- *intralayer* subatomic continuous displacement disorder (statistical distribution of near-neighbor distances), characterized by a Gaussian standard deviation σ_W, σ_{Cu} for each constituent layer.
- *interface roughness* (intermixing), as modeled by a shifted Poisson distribution of the layer thicknesses centered on their nominal values, describing the crenelated interfaces.

These two independent statistical parameters give a very good account of the observed diffraction patterns. The intralayer continuous disorder attenuates the satellite intensities. The same effect is produced by the interface roughness, which additionally blurs also the size oscillations. However, additional information about the in-plane structure of the interface, such as the dimension of planar domains and other in-plane correlations, cannot be extracted from Bragg–Brentano measurements, as they probe the sample only along the direction normal to its surface.

In the Fig. 4, the XRD scans of tensile and compressive NMLs are shown and compared with the model calculations. The satellite peaks, typical of a superlattice structure [41,68], are very distinct in the compressive NML, but hardly discernible in the tensile NML. This indicates a higher level of interface disorder in the tensile NMLs. The calculated XRD scans, which reproduce accurately the experimental ones, are obtained by adjusting the parameters for internal and interface disorder as described above. As follows from the model fit, the disorder within the W layers is 3 times higher in the tensile NML, whereas the Cu layer disorder is comparable for the two cases. The information about the interface is contained in the standard deviation $\Sigma = \sqrt{\mu}$, where μ is the expected value of the shifted Poisson distribution. This information is only about the global average displacement (in units of lattice planes along the growth direction) of the interface with respect to the position of the plane corresponding to the nominal thickness N. With μ and N, it is possible to define a dimensionless roughness parameter, $\mathrm{R} = \sqrt{\mu/2}/\mathrm{N}$. Even in this case, the roughness at the interface is more than 3 times higher for the tensile multilayers. The structural disorder analysis by XRD is in excellent agreement with the cross-sectional STEM analysis, both indicating sharper and less intermixed interfaces in the compressive NML as compared to the tensile one.

In the inbox of Fig. 4, the values of strain derived with the model are also reported. They are defined as the difference from the bulk values of the interplanar distance in the out-of-plane direction. Since the out-of-plane direction is (111) for Cu and (110) for W, ϵ_{Cu} and ϵ_W are defined as: $\epsilon_{Cu} = \frac{d_{(111),\mathrm{Cu}} - d^{\mathrm{th}}_{(111),\mathrm{Cu}}}{d^{\mathrm{th}}_{(111),\mathrm{Cu}}}$ and $\epsilon_W = \frac{d_{(110),\mathrm{W}} - d^{\mathrm{th}}_{(110),\mathrm{W}}}{d^{\mathrm{th}}_{(110),\mathrm{W}}}$ with $d^{\mathrm{th}}_{(111),\mathrm{Cu}} = 2.087$ Å [69] and $d^{\mathrm{th}}_{(110),\mathrm{W}} = 2.238$ Å [70].

3.2. Annealed Cu/W NMLs

3.2.1. Microstructure by cross-sectional SEM and XPS depth profiling

NMLs are associated with high excess Gibbs energies as originating from the very high-density of internal interfaces (i.e., grain and phase boundaries), as well as from internal stress gradients [4,71]. Consequently, NMLs are generally prone to degradation upon high temperature annealing [17,41,42,72,73]. In the following, the effect of the stress state and microstructure on the thermal stability of the compressive and tensile Cu/W NMLs is investigated by SEM and XPS. The tensile and compressive Cu/W NMLs were annealed in vacuum for 100 min at a temperature of 300 °C, 600 °C, 800 °C or, 850 °C. The results of the cross-sectional SEM analysis of the as-deposited and annealed microstructures are shown in Fig. 5. The experimental observations are discussed in relation to previous findings on the thermal stability of Cu/W NMLs reported in the literature.

SEM analysis of the as-deposited NMLs also indicates that the atomic disorder is higher for the tensile NML (compare Fig. 5a and b). In particular, the contrast between the bright W and dark Cu interlayers (in backscattered electron mode) is better resolved for the compressive NMLs, suggesting sharper Cu/W interfaces as compared to the tensile NMLs. As reflected by SEM analysis of the as-deposited NML surfaces (see Fig. S4), the tensile NML has a higher surface roughness and its intersecting grain boundary (GB) network with the surface appears more open (as compared to the compressive NML), which is consistent with the predicted effect of stress on the GB shape [74]. The atomic disorder of the ten-

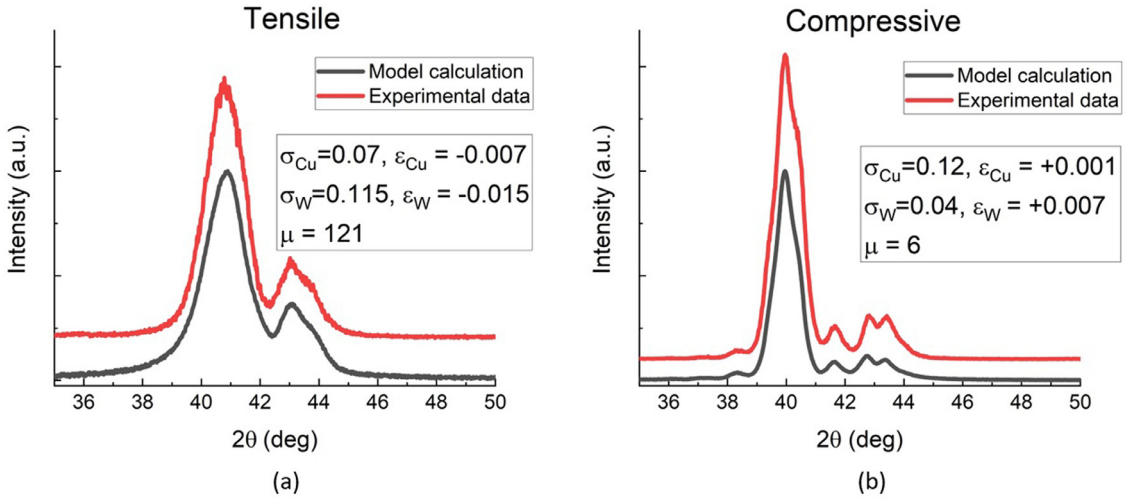

Fig. 4. XRD on (a) tensile and (b) compressive multilayers compared to the model calculation. The parameters used in the model are also indicated.

sile NML appears to be reduced after annealing in the range from 300 °C to 600 °C (Fig. 5b, d, and f), whereas such an effect is not discernible by SEM for the compressive NML (Fig. 5a, c, and e). At 800 °C, a striking difference in thermal stability between the tensile and compressive NML becomes evident: while the tensile NML has completely transformed into a nanocomposite (NC), the compressive NML is still in the first stage of NML degradation (compare Fig. 5g and h).

A compressive NML sample was also annealed at an even higher temperature of 850 °C, revealing that the NML-to-NC transformation process is still ongoing and has only partially completed: see Fig. 5i. Interestingly, the partially transformed compressive Cu/W NML annealed at 850 °C shows more pronounced layer degradation with grain coarsening of W towards the bottom of the NML stack. As suggested from the roughly triple increase of the thickness of the W buffer layer after the annealing (compare Fig. 5a and i), the NML-to-NC transformation is accompanied by coalesence of W grains from the NML with underlying grains of the W buffer layer. More pronounced grain coarsening of W at the bottom of the NML stack is also observed for the fully transformed tensile NML annealed at 800 °C (see Fig. 5h). Such thickening of the W buffer layer by grain coarsening requires movement of Cu towards the upper part of the NML layer stack, which indeed already occurs at temperatures as low as 400–500 °C [41,42].

XPS sputter-depth profiles of the as-deposited (Fig. 6a and b) and annealed (Fig. 6c and d) compressive and tensile NMLs confirm the cross-sectional SEM analyses. Regular oscillations of the Cu and W signals, as originating from the alternating Cu and W nanolayers in the NML stack, are clearly resolved in the sputter-depth profiles of the as-prepared NMLs. These oscillations are more pronounced for the compressive NML, since they are less disordered and have sharper Cu/W interfaces. The higher degree of disorder in the tensile NMLs should be associated with a lower overall atomic density, which also rationalizes the higher sputter rate of as-deposited tensile NML: i.e., for the applied Ar^+ sputter voltage of 1 kV, total sputter times of 70 and 80 min are required to reach the $a-SiN_x$ substrate interlayer for the as-deposited tensile and compressive NML, respectively (compare Fig. 6a and b). Notably, the O and C contents within the as-deposited NMLs are below 1 at.%. After the annealing at 800 °C, the sputter-depth profile of the compressive NML still exhibits distinct oscillations of the Cu and W signals (albeit a bit more damped as compared to the as-deposited NML). These oscillations are completely damped for the tensile NML annealed at 800 °C, in agreement with the completed NML-to-NC transformation observed by SEM (see Fig. 5h).

As reported in previous studies on the thermal stability of Cu/W NMLs [17,41,42,72,75], the thermal degradation of Cu/W NMLs is a diffusion-controlled process, which becomes thermally activated in the temperature range of 650 - 800 °C (depending on the as-deposited microstructure, in accordance with SEM and XPS analyses in the present study). The onset of NML degradation is initiated by GB grooving [17,42]. The GB grooving kinetics are rate-limited by short-circuit diffusion of W along Cu/W interfaces and/or W GBs [17,41]. Thermal grooving of the W GBs by Cu progresses with increasing annealing time and eventually causes layer pinch-off (due to the merging of opposite GB grooves), as also evidenced in Fig. 5g. After prolonged annealing, the NML is transformed into a NC composed of globular W particles embedded in a Cu matrix [13,17,41,76], as observed in Fig. 5h. During the course of the NML-to-NC transformation, the system tends to gradually release its strain energy associated with intrinsic stresses [42]. Stress relaxation is initiated by the outflow of Cu to the NML surface at temperatures as low as 400–500 °C [41,42]. As reported in Ref. [72], the onset of the NML-to-NC transformation process coincides with the complete relaxation of interface stresses in the Cu/W NML stack (*note*: the interface stresses associated with incoherent Cu(111)/W(110) interfaces in as-deposited Cu/W NMLs are relatively high).

Noteworthy, XPS depth profiling of the vacuum-annealed NMLs evidences inward diffusion of oxygen into the NML stack during vacuum annealing at 800 °C, reaching an O content of roughly 5 at.% in the interior of the annealed NMLs: see Fig. 6c and d. Inward diffusion of O into NML stacks upon annealing in air and inert Ar atmospheres has also been observed for other NML systems, such as Ag/AlN [77] and AgCu/AlN [3]. These previous studies have concluded that O penetrates along the GBs of the AlN barrier layers. Notably, for the compressive NML, the O diffusion profile still exhibits some oscillations (i.e. the O content is slightly higher in the W interlayers as compared to the adjacent Cu interlayers), whereas the O diffusion profile is gradual and smooth for the tensile NML. Indeed, the W interlayers of the compressive NML are only partially pinched off after the annealing at 800 °C, whereas the tensile NML has already fully transformed into a NC. As demonstrated in Ref. [76], the relaxation of compressive intrinsic stresses in the W interlayers during high-temperature annealing will lower the energy barriers for diffusion of W and of foreign atoms (like Cu and O) along the W GBs. Consequently, stress relax-

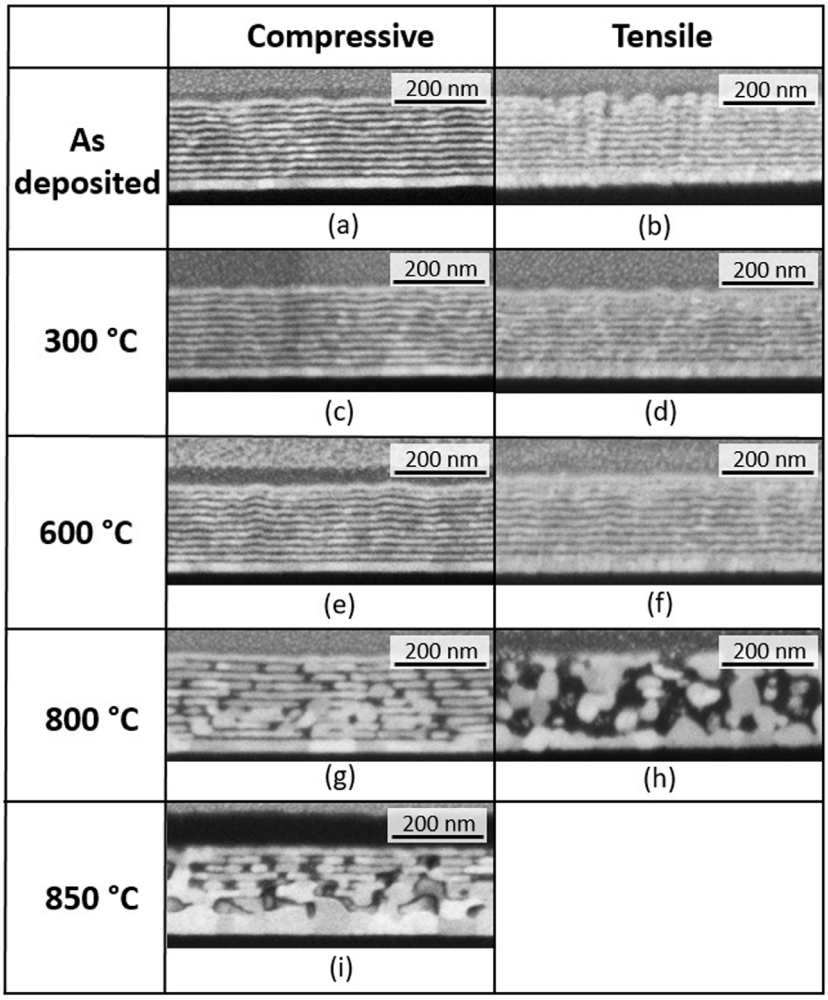

Fig. 5. SEM images of cross sections of as-deposited and annealed compressive NMLs (a), (c), (e), (g), (i) and tensile NMLs (b), (d), (f) and (h). Bright regions in the NML/NC are associated to W; dark regions to Cu.

ation at the onset of the NML-to-NC transformation will promote short-circuit inward diffusion of O (in addition to Cu and W) along W GBs during vacuum-annealing (being more pronounced for the tensile Cu/W NML due to its more open GB structure).

As concluded on the basis of the SEM and XPS analyses of as-deposited and annealed Cu/W NMLs with different initial stress states, NML-to-NC transformation can be shifted to significantly lower temperatures by producing Cu/W NMLs with less compressive stress and more structural disorder in the NML stack. In general, the disordered microstructure, as in the tensile NMLs, can facilitate atomic mobility at high temperature and hence promote the NML-to-NC transformation. In addition, atomic diffusion can be affected also by stress [76].

3.2.2. Stress state and structural disorder by XRD

XRD scans of the tensile and compressive multilayers, as acquired after different annealing temperatures, are shown in Fig. 7a and b, respectively. The tensile NML is completely degraded into a nanocomposite at 800 °C (see Fig. 5h). On the contrary, the compressive NML still shows intensity modulations after the annealing at 800 °C, i.e., satellite peaks, typical of a periodic structure, in accordance with the SEM observations (see Fig. 5g). Even for a slightly higher annealing temperature of 850 °C, the XRD diffractogram of the compressive NML still shows satellites peaks, although strongly reduced in intensity, indicative of an incomplete nanocomposite transformation (see Fig. 5i). Notably, the tensile system provides evidence of an increase of the satellite modulation intensity at 600 °C, which suggests an increase in the interface coherency upon annealing, in agreement with the SEM observations (see above). Such a thermally activated increase in interface coherency (as driven by a reduction of the interface energy) is commonly observed for magnetron-sputtered NMLs [17,41,72,75,76].

The corresponding internal stress evolution is shown in Fig. 7c. Here, it is emphasized that the residual stresses were acquired after cooling down to room temperature (RT). Accordingly, a stress-free state at RT not necessarily implies a stress-free state at the respective annealing temperature. Namely, the different thermal expansion coefficients of W, Cu and the Si substrate may impose thermal stresses on Cu and W during cooling [42]. In this regard, it is noted that the thermal mismatch between W and Si is relatively small and therefore any thermal stress contribution in W during cooling can be neglected, which is not necessarily the case for Cu [42].

While the compressive NML gradually relaxes the intrinsic compressive stresses in the W interlayers until 800 °C, the tensile NML has already largely relaxed its intrinsic tensile stresses in W at 600 °C. The Cu interlayers reach a similar, low tensile stress level for the compressive and tensile NML after annealing at 300 °C. Strikingly, the tensile NML annealed at 600 °C again shows a higher tensile stress (after cooling down to RT). It may be assumed that the Cu stresses are largely relaxed during the heating at 600 °C or higher [42] and the tensile stress contributions in Cu

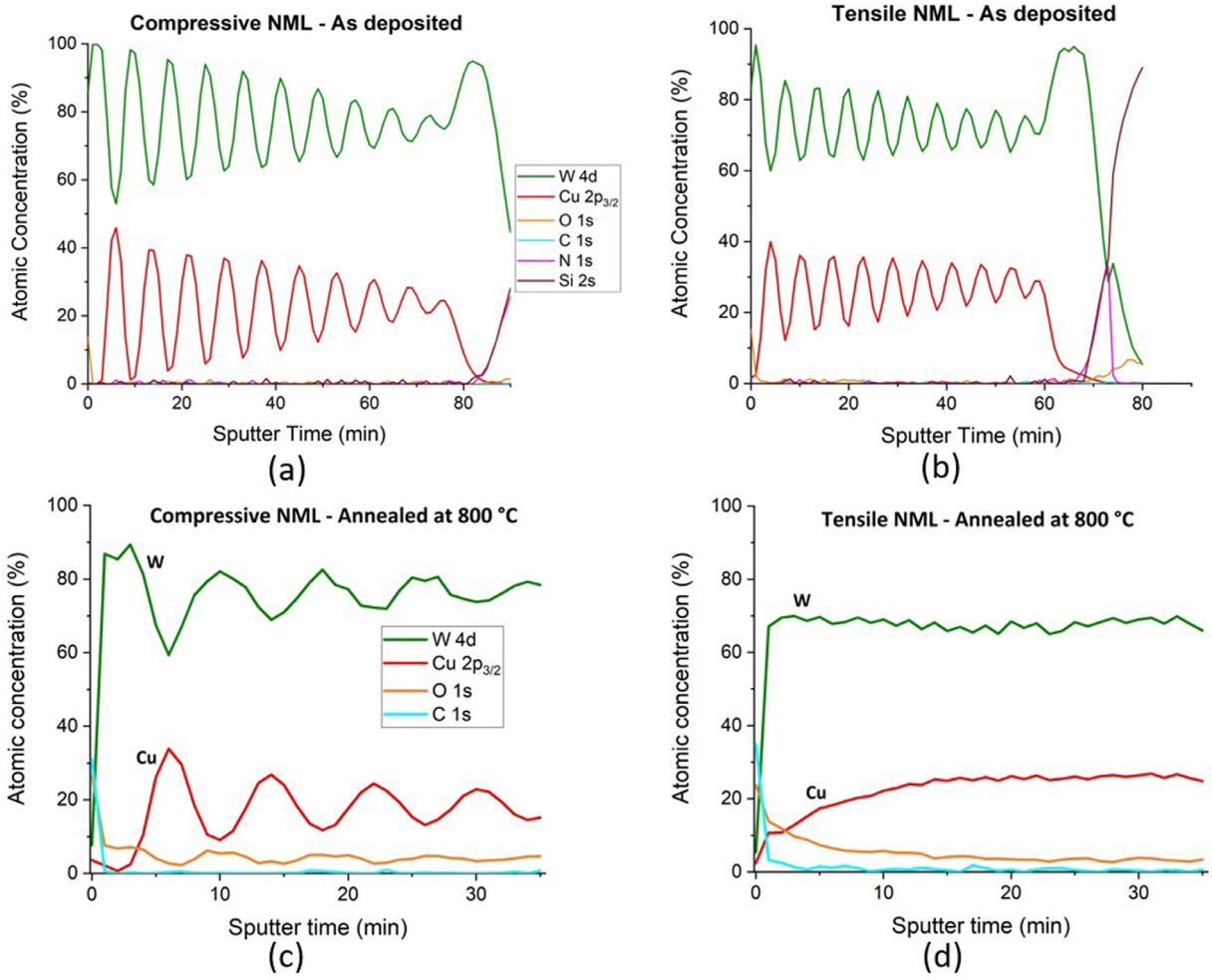

Fig. 6. XPS sputter depth profiles of Cu/W NMLs (a) as-deposited compressive, (b) as-deposited tensile, (c) compressive annealed at 800 °C, and (d) tensile annealed at 800 °C.

thus mainly originate from the cooling stage (since Cu has a higher thermal expansion coefficient than W and Si). The coherency of the Cu/W interface of the tensile NMLs is enhanced upon annealing at 600 °C, as shown in Fig. 7a, where the finite size oscillations are more pronounced, denoting sharp and less defective interfaces. This fact, together with the higher thermal stresses upon cooling (with respect to 300 °C) explains the higher tensile stress in Cu layers measured at 600 °C. At 800 °C, instead, the tensile system is completely destroyed into a nanocomposite and behaves as a whole material with its own thermal expansion coefficient, which is lower than the one of Cu. Indeed, stresses measured in W and Cu are the same and both are tending towards relaxation. Similar trends are observed also in compressive NMLs, but at higher temperatures, since the transition into NC requires more thermal energy to occur.

The stress relaxation process is also evidenced by the XRD model analysis performed on the satellite peaks as a function of annealing temperature. In Fig. 8, the parameters extracted from the XRD model are plotted as a function of the annealing temperature. The corresponding simulations for the compressive and tensile NMLs after annealing at different temperatures are provided in Fig. S5 of the Supplementary material. The thus obtained values of the Poisson parameter, μ, describing the interface roughness and of σ_W, representing the intralayer atomic displacement, do not change considerably with temperature for the compressive NML (Fig. 8); only at 800 °C, the μ value starts to increase, denoting a more pronounced interface disorder at the onset of the nanocomposite transformation (see also Section 3.2.1). For the tensile NML, both the interface roughness and the W intralayer σ disorder decrease with increasing annealing temperature up to 600 °C, in accordance with the sharping of the Cu/W interfaces by SEM and the more pronounced interface coherency by XRD up to 600 °C (see above). At 800 °C, the tensile NML is completely transformed into a nanocomposite and therefore the XRD model cannot be applied; consequently, μ and σ_W values for the tensile NML can only be derived up to 600 °C.

3.3. Thermal conductivity

In the following, the effect of interface disorder and layer microstructure of the tensile and compressive NMLs in their as-deposited and annealed states is correlated to the thermal conductivity, which is a key property for application (see Introduction). The TDTR-measured thermal conductivity of the as-deposited tensile NML is 9.1 ± 0.98 W m^{-1} K^{-1}. The thermal conductivity of the as-deposited compressive NML, on the other hand, is measured to be 22.9 ± 4.6 W m^{-1} K^{-1}, nearly 2.5 times higher compared to the tensile NML. The uncertainty of the TDTR measurements here incorporates the measurement repeatability, uncertainty of the Al thickness (2 nm), NML heat capacity (5%), and thermal conductivity of the Al, W, Si_3N_4, and Si layers (10%). The difference in cross-plane thermal conductivity between the tensile and compressive specimens in the as-deposited state can be directly correlated to microstructure. As discussed earlier, the W layers of the tensile

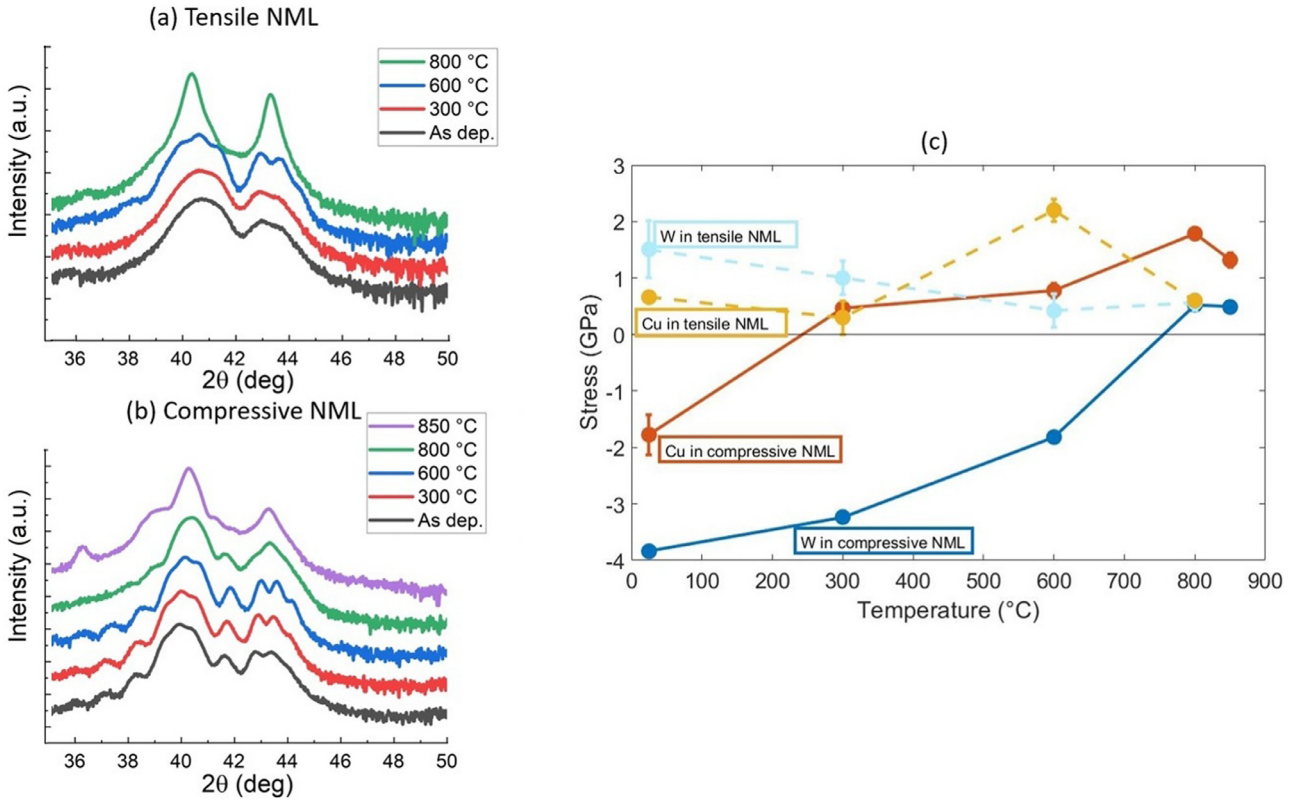

Fig. 7. (a) XRD θ-2θ scans of tensile NMLs as deposited and annealed at 300 °C, 600 °C and 800 °C; (b) XRD θ-2θ scans of compressive NMLs as deposited and annealed at 300 °C, 600 °C, 800 °C and 850 °C; (c) Stress evolution upon annealing measured by XRD at room temperature. For some points the error bars are not visible because they are smaller than the circle symbol.

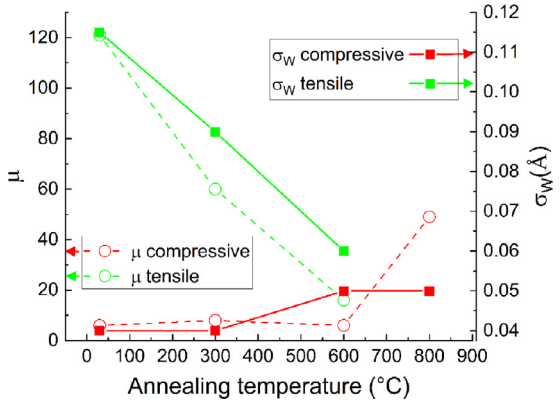

Fig. 8. Poisson disorder distribution related to interface roughness plotted for compressive and tensile nanomultilayers annealed at different temperatures (left axis, dashed lines). The corresponding W intralayer disorder σ for both multilayers is also shown on the right axis (continuous lines).

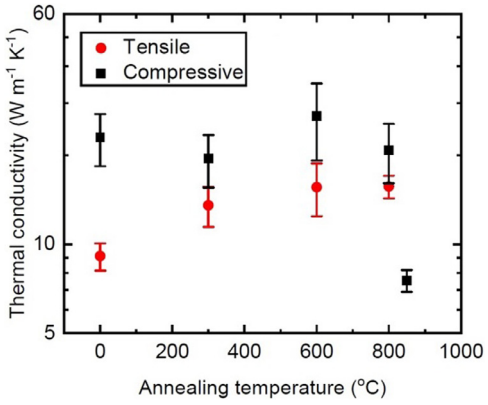

Fig. 9. Thermal conductivity of the tensile and compressive samples as a function of annealing temperature.

NML are much more disordered compared to the W layers of the compressive NML (see Section 3.1.2). The interfacial roughness of the tensile NML is also much higher than that of the compressive NML. Moreover, the tensile NML has a smaller grain size (see STEM characterization in Fig. 2 and related discussion). The structure disorder and smaller grain size result in a significantly lower thermal conductivity of the as-deposited tensile NML [13,54,78–81].

The thermal conductivity of the tensile and compressive specimens after annealing at different temperatures was also measured (after cooling down to RT): see Fig. 9. Within the uncertainty of the measurement, the thermal conductivity of the compressive NML remains approximately constant up to 800 °C, followed by a sharp decrease at 850 °C. Indeed, the compressive NML remains stable up to 800 °C. The NML-to-NC transformation sets in at $T > 800$ °C and is partially completed after the annealing at 850 °C. The nanocomposite structure introduces additional electron and phonon scattering mechanisms, resulting in a substantial decrease of the thermal conductivity [82–85]. A completely different trend is observed for the tensile NML. The thermal conductivity of the tensile NML gradually increases with annealing temperature, which is attributed to the reduction of atomic disorder (see Section 3.2.1). Cancellieri et al. [13] also noticed a similar thermal conductivity increase during the NML-to-NC transformation; however, contrary to this work, the stress state was not defined. Therefore, the findings of our

Table 2
Total resistance between the Al transducer and the Si substrate, *R*th, for the as-deposited and annealed (at 600 °C) Cu/W nanomultilayers, as derived by SSTR and TDTR.

Specimen	*R*th value (m^2 K GW^{-1})	
	SSTR	TDTR
Tensile as-deposited	71 ± 14.9	79 ± 9
Compressive as-deposited	64.5 ± 12.7	70 ± 9.1
Tensile annealed at 600 °C	78.1± 14.8	75.7 ± 8.9
Compressive annealed at 600 °C	67.1± 14.8	73.5 ± 9.2

study are crucial for correlating stress state, microstructure and thermal properties of Cu/W NMLs.

The total resistance between the Al transducer and the Si substrate (i.e., the *R*th value) was also measured by SSTR for the as-deposited and NMLs annealed at 600 °C. The results are presented in Table 2; the error bars represent the measurement repeatability, the uncertainty of the experimental proportionality constant, as well as the Al transducer and Si substrate thermal conductivities. The *R*th values derived from the SSTR measurements can be compared to the corresponding *R*th values obtained by TDTR (see Table 2). The *R*th values derived independently by SSTR and TDTR are in excellent agreement (within the uncertainty of both measurement methods) and nearly the same for the selected samples, despite the vastly different microstucture and thermal conductivity of the different Cu/W NML variants. This indicates that the contribution of the Cu/W multilayers to the total resistance, *R*th, is relatively small. This suggests that the thermal performance of a NML device or functional component with a similar geometry will not be significantly impacted by the stresses and microstructure generated during fabrication. However, such intrinsic stresses and microstructure will adversely impact the thermal stability and, thereby, the device lifetime.

4. Conclusions

Cu/W nanomultilayers (NMLs) have been deposited by DC magnetron sputtering and their stress state and microstructure have been tuned by acting on the deposition parameters. On one hand, high Ar-pressure and low gun power favor the development of a tensile stress, a disordered microstructure, and intermixing at the interfaces. On the other hand, NMLs produced under low Ar-pressure and high gun power display a compressive stress and a dense and compact structure with sharp interfaces. The stress state and the microstructure have been observed to affect the thermal stability and thermal conductivity of the NMLs. The compressive system has manifested overall better performance: its thermal conductivity is 2.5 times higher than that of the tensile system in the as-deposited state. This number directly scales with the internal positional atomic disorder which is also $\sim$ 3 times higher in the tensile samples. Additionally, the compressive sample is thermally more stable and it requires much higher annealing temperatures to turn into a nanocomposite. Although the thermal conductivity of the tensile sample improves with annealing, it underperforms the compressive sample until 800 °C. Despite these advantages of the compressive NML, the tensile NML can be appealing in applications such as brazing, where the transition from NML to NC is desirable at lower temperatures. Therefore, our study can provide guidelines for adequately choosing the deposition parameters to significantly reduce the brazing temperature and thereby, the cost. However, for such joining applications, a trade-off between different properties must be found, since the stress state and the microstructure are intrinsically bounded. The critical interplay between the internal stress and microstructure was clearly shown in relation to properties like thermal stability and thermal conductivity. This work paves the way to establish a link between nanoscale interface structure and physical properties in multilayer systems towards an optimized microstructure for targeted applications.

Data availability

The data that support the findings of this study are openly available in Zenodo at http://doi.org/10.5281/zenodo.7039958, Ref. [86]. Other data are available upon reasonable request.

Declaration of Competing Interest

The authors declare that they have no known competing financial interests or personal relationships that could have appeared to influence the work reported in this paper.

Acknowledgments

G.L. acknowledges the Swiss National Science Foundation (SNSF), project number 200021_192224 for financially supporting this research. The authors acknowledge also SNSF research equipment (R'Equip) grant no.182987 for co-financing the photoemission setup. M.S.B.H., E.R.H., J.A.T., and P.E.H acknowledges financial support from the Semiconductor Research Corporation, Grant number 2021-NM-3047 and the Army Research Office, Grant number W911NF-16-1-0406. The authors would like to thank Sean W. King for helpful discussions. T. Burgdorf and H.R. Elsener are acknowledged for their support with the high temperature treatments.

Supplementary material

Supplementary material associated with this article can be found, in the online version, at doi:10.1016/j.actamat.2022.118315.

References

[1] J. Janczak-Rusch, G. Kaptay, L. Jeurgens, Interfacial design for joining technologies: an historical perspective, J. Mater. Eng. Perform. 23 (5) (2014) 1608–1613, doi:10.1007/s11665-014-0928-5.
[2] G. Kaptay, J. Janczak-Rusch, G. Pigozzi, L. Jeurgens, Theoretical analysis of melting point depression of pure metals in different initial configurations, J. Mater. Eng. Perform. 23 (5) (2014) 1600–1607, doi:10.1007/s11665-014-0885-z.
[3] J. Janczak-Rusch, M. Chiodi, C. Cancellieri, F. Moszner, R. Hauert, G. Pigozzi, L. Jeurgens, Structural evolution of Ag–Cu nano-alloys confined between AlN nano-layers upon fast heating, Phys. Chem. Chem. Phys. 17 (42) (2015) 28228–28238, doi:10.1039/C5CP00782H.
[4] G. Kaptay, J. Janczak-Rusch, L. Jeurgens, Melting point depression and fast diffusion in nanostructured brazing fillers confined between barrier nanolayers, J. Mater. Eng. Perform. 25 (8) (2016) 3275–3284, doi:10.1007/s11665-016-2123-3.
[5] O. Auciello, S. Chevacharoenkul, M. Ameen, J. Duarte, Controlled ion beam sputter deposition of W/Cu/W layered films for microelectronic applications, J. Vac. Sci. Technol. A 9 (3) (1991) 625–631, doi:10.1116/1.577377.
[6] M. Takeyama, A. Noya, T. Fukuda, Thermal stability of Cu/W/Si contact systems using layers of Cu (111) and W (110) preferred orientations, J. Vac. Sci. Technol. A 15 (2) (1997) 415–420, doi:10.1116/1.580500.
[7] H. Ono, T. Nakano, T. Ohta, Diffusion barrier effects of transition metals for Cu/M/Si multilayers (M = Cr, Ti, Nb, MO, Ta, W), Appl. Phys. Lett. 64 (12) (1994) 1511–1513, doi:10.1063/1.111875.
[8] K.T. Nam, A. Datta, S.-H. Kim, K.-B. Kim, Improved diffusion barrier by stuffing the grain boundaries of TiN with a thin Al interlayer for Cu metallization, Appl. Phys. Lett. 79 (16) (2001) 2549–2551, doi:10.1063/1.1409594.
[9] S.-H. Kim, K.T. Nam, A. Datta, H.-M. Kim, K.-B. Kim, D.-H. Kang, Multilayer diffusion barrier for copper metallization using a thin interlayer metal (M = Ru, Cr, and Zr) between two TiN films, J. Vac. Sci. Technol. B 21 (2) (2003) 804–813, doi:10.1116/1.1562645.
[10] D. Gall, The search for the most conductive metal for narrow interconnect lines, J. Appl. Phys. 127 (5) (2020) 050901, doi:10.1063/1.5133671.
[11] S. Anders, A. Anders, J. Kortright, K.M. Yu, I. Brown, I. Ivanov, Vacuum arc deposition of multilayer X-ray mirrors, Surf. Coat. Technol. 61 (1–3) (1993) 257–261, doi:10.1016/0257-8972(93)90235-G.
[12] M. Stueber, H. Holleck, H. Leiste, K. Seemann, S. Ulrich, C. Ziebert, Concepts for the design of advanced nanoscale PVD multilayer protective thin films, J. Alloys Compd. 483 (1–2) (2009) 321–333, doi:10.1016/j.jallcom.2008.08.133.

[13] C. Cancellieri, E.A. Scott, J. Braun, S.W. King, R. Oviedo, C. Jezewski, J. Richards, F. La Mattina, L.P. Jeurgens, P.E. Hopkins, Interface and layer periodicity effects on the thermal conductivity of copper-based nanomultilayers with tungsten, tantalum, and tantalum nitride diffusion barriers, J. Appl. Phys. 128 (19) (2020) 195302, doi:10.1063/5.0019907.

[14] Y. Gao, T. Yang, J. Xue, S. Yan, S. Zhou, Y. Wang, D.T. Kwok, P.K. Chu, Y. Zhang, Radiation tolerance of Cu/W multilayered nanocomposites, J. Nucl. Mater. 413 (1) (2011) 11–15, doi:10.1016/j.jnucmat.2011.03.030.

[15] C. Wang, P. Brault, C. Zaepffel, J. Thiault, A. Pineau, T. Sauvage, Deposition and structure of W–Cu multilayer coatings by magnetron sputtering, J. Phys. D 36 (21) (2003) 2709, doi:10.1088/0022-3727/36/21/018.

[16] S. Wen, R. Zong, F. Zeng, Y. Gao, F. Pan, Evaluating modulus and hardness enhancement in evaporated Cu/W multilayers, Acta Mater. 55 (1) (2007) 345–351, doi:10.1016/j.actamat.2006.07.043.

[17] F. Moszner, C. Cancellieri, M. Chiodi, S. Yoon, D. Ariosa, J. Janczak-Rusch, L. Jeurgens, Thermal stability of Cu/W nano-multilayers, Acta Mater. 107 (2016) 345–353, doi:10.1016/j.actamat.2016.02.003.

[18] L. Dong, G. Wei, T. Cheng, J. Tang, X. Ye, M. Hong, L. Hu, R. Yin, S. Zhao, G. Cai, et al., Thermal conductivity, electrical resistivity, and microstructure of Cu/W multilayered nanofilms, ACS Appl. Mater. Interfaces 12 (7) (2020) 8886–8896, doi:10.1021/acsami.9b21182.

[19] A. Brenner, S. Senderoff, Calculation of stress in electrodeposits from the curvature of a plated strip, J. Res. Natl. Bur. Stand. 42 (105) (1949) 105–123.

[20] H. Murbach, H. Wilman, The origin of stress in metal layers condensed from the vapour in high vacuum, Proc. Phys. Soc. Lond. Sect. B 66 (11) (1953) 905, doi:10.1088/0370-1301/66/11/301.

[21] R. Hoffman, R. Daniels, E. Crittenden, The cause of stress in evaporated metal films, Proc. Phys. Soc. Lond. Sect. B 67 (6) (1954) 497, doi:10.1088/0370-1301/67/6/110.

[22] H. Story, R. Hoffman, Stress annealing in vacuum deposited copper films, Proc. Phys. Soc. Lond. Sect. B 70 (10) (1957) 950, doi:10.1088/0370-1301/70/10/305.

[23] R. Koch, The intrinsic stress of polycrystalline and epitaxial thin metal films, J. Phys. 6 (45) (1994) 9519, doi:10.1088/0953-8984/6/45/005.

[24] G. Abadias, E. Chason, J. Keckes, M. Sebastiani, G.B. Thompson, E. Barthel, G.L. Doll, C.E. Murray, C.H. Stoessel, L. Martinu, Stress in thin films and coatings: current status, challenges, and prospects, J. Vac. Sci. Technol. A 36 (2) (2018) 020801, doi:10.1116/1.5011790.

[25] R. Abermann, R. Koch, The internal stress in thin silver, copper and gold films, Thin Solid Films 129 (1–2) (1985) 71–78, doi:10.1016/0040-6090(85)90096-3.

[26] G. Thurner, R. Abermann, Internal stress and structure of ultrahigh vacuum evaporated chromium and iron films and their dependence on substrate temperature and oxygen partial pressure during deposition, Thin Solid Films 192 (2) (1990) 277–285, doi:10.1016/0040-6090(90)90072-L.

[27] T. Vink, M. Somers, J. Daams, A. Dirks, Stress, strain, and microstructure of sputter-deposited Mo thin films, J. Appl. Phys. 70 (8) (1991) 4301–4308, doi:10.1063/1.349108.

[28] J. Hinze, K. Ellmer, In situ measurement of mechanical stress in polycrystalline zinc-oxide thin films prepared by magnetron sputtering, J. Appl. Phys. 88 (5) (2000) 2443–2450, doi:10.1063/1.1288162.

[29] G. Abadias, L.E. Koutsokeras, P. Guerin, P. Patsalas, Stress evolution in magnetron sputtered Ti–Zr–N and Ti–Ta–N films studied by in situ wafer curvature: role of energetic particles, Thin Solid Films 518 (5) (2009) 1532–1537, doi:10.1016/j.tsf.2009.07.183.

[30] H. Liu, G. Tang, F. Zeng, F. Pan, Influence of sputtering parameters on structures and residual stress of AlN films deposited by DC reactive magnetron sputtering at room temperature, J. Cryst. Growth 363 (2013) 80–85, doi:10.1016/j.jcrysgro.2012.10.008.

[31] J. Ruud, A. Witvrouw, F. Spaepen, Bulk and interface stresses in silver-nickel multilayered thin films, J. Appl. Phys. 74 (4) (1993) 2517–2523, doi:10.1063/1.354692.

[32] A.L. Shull, F. Spaepen, Measurements of stress during vapor deposition of copper and silver thin films and multilayers, J. Appl. Phys. 80 (11) (1996) 6243–6256, doi:10.1063/1.363701.

[33] J. Bain, L. Chyung, S. Brennan, B. Clemens, Elastic strains and coherency stresses in Mo/Ni multilayers, Phys. Rev. B 44 (3) (1991) 1184, doi:10.1103/PhysRevB.44.1184.

[34] G. Lorenzin, L.P. Jeurgens, C. Cancellieri, Stress tuning in sputter-grown Cu and W films for Cu/W nanomultilayer design, J. Appl. Phys. 131 (22) (2022) 225304, doi:10.1063/5.0088203.

[35] E. Gilardi, A. Fluri, T. Lippert, D. Pergolesi, Real-time monitoring of stress evolution during thin film growth by in situ substrate curvature measurement, J. Appl. Phys. 125 (8) (2019) 082513, doi:10.1063/1.5054092.

[36] G. Abadias, P. Guerin, In situ stress evolution during magnetron sputtering of transition metal nitride thin films, Appl. Phys. Lett. 93 (11) (2008) 111908, doi:10.1063/1.2985814.

[37] G.G. Stoney, The tension of metallic films deposited by electrolysis, Proc. R. Soc. Lond. Ser. A 82 (553) (1909) 172–175, doi:10.1098/rspa.1909.0021.

[38] G.C. Janssen, M. Abdalla, F. Van Keulen, B. Pujada, B. Van Venrooy, Celebrating the 100th anniversary of the stoney equation for film stress: developments from polycrystalline steel strips to single crystal silicon wafers, Thin Solid Films 517 (6) (2009) 1858–1867, doi:10.1016/j.tsf.2008.07.014.

[39] B. Clemens, J. Bain, Stress determination in textured thin films using X-ray diffraction, MRS Bull. 17 (7) (1992) 46–51, doi:10.1557/S0883769400041658.

[40] U. Welzel, J. Ligot, P. Lamparter, A. Vermeulen, E. Mittemeijer, Stress analysis of polycrystalline thin films and surface regions by X-ray diffraction, J. Appl. Crystallogr. 38 (1) (2005) 1–29, doi:10.1107/S0021889804029516.

[41] A. Druzhinin, D. Ariosa, S. Siol, N. Ott, B. Straumal, J. Janczak-Rusch, L. Jeurgens, C. Cancellieri, Effect of the individual layer thickness on the transformation of Cu/W nano-multilayers into nanocomposites, Materialia 7 (2019) 100400, doi:10.1016/j.mtla.2019.100400.

[42] C. Cancellieri, F. Moszner, M. Chiodi, S. Yoon, J. Janczak-Rusch, L. Jeurgens, The effect of thermal treatment on the stress state and evolving microstructure of Cu/W nano-multilayers, J. Appl. Phys. 120 (19) (2016) 195107, doi:10.1063/1.4967992.

[43] D.G. Cahill, Analysis of heat flow in layered structures for time-domain thermoreflectance, Rev. Sci. Instrum. 75 (12) (2004) 5119–5122, doi:10.1063/1.1819431.

[44] A.J. Schmidt, X. Chen, G. Chen, Pulse accumulation, radial heat conduction, and anisotropic thermal conductivity in pump-probe transient thermoreflectance, Rev. Sci. Instrum. 79 (11) (2008) 114902, doi:10.1063/1.3006335.

[45] J.P. Feser, J. Liu, D.G. Cahill, Pump-probe measurements of the thermal conductivity tensor for materials lacking in-plane symmetry, Rev. Sci. Instrum. 85 (10) (2014) 104903, doi:10.1063/1.4897622.

[46] P. Jiang, X. Qian, R. Yang, Tutorial: time-domain thermoreflectance (TDTR) for thermal property characterization of bulk and thin film materials, J. Appl. Phys. 124 (16) (2018) 161103, doi:10.1063/1.5046944.

[47] K. Ye, S.C. Siah, P.T. Erslev, A. Akey, C. Settens, M.S.B. Hoque, J. Braun, P. Hopkins, G. Teeter, T. Buonassisi, et al., Tuning electrical, optical, and thermal properties through cation disorder in Cu2ZnSnS4, Chem. Mater. 31 (20) (2019) 8402–8412, doi:10.1021/acs.chemmater.9b02287.

[48] A. Giri, A.Z. Chen, A. Mattoni, K. Aryana, D. Zhang, X. Hu, S.-H. Lee, J.J. Choi, P.E. Hopkins, Ultralow thermal conductivity of two-dimensional metal halide perovskites, Nano Lett. 20 (5) (2020) 3331–3337, doi:10.1021/acs.nanolett.0c00214.

[49] D.H. Olson, J.T. Gaskins, J.A. Tomko, E.J. Opila, R.A. Golden, G.J. Harrington, A.L. Chamberlain, P.E. Hopkins, Local thermal conductivity measurements to determine the fraction of α-cristobalite in thermally grown oxides for aerospace applications, Scr Mater. 177 (2020) 214–217, doi:10.1016/j.scriptamat.2019.10.027.

[50] G.K. White, S. Collocott, Heat capacity of reference materials: Cu and W, J. Phys. Chem. Ref. Data 13 (4) (1984) 1251–1257, doi:10.1063/1.555728.

[51] J. Hostetler, A. Smith, P. Norris, Thin-film thermal conductivity and thickness measurements using picosecond ultrasonics, Microscale Thermophys. Eng. 1 (3) (1997) 237–244, doi:10.1080/108939597200250.

[52] E.A. Scott, J.T. Gaskins, S.W. King, P.E. Hopkins, Thermal conductivity and thermal boundary resistance of atomic layer deposited high-k dielectric aluminum oxide, hafnium oxide, and titanium oxide thin films on silicon, APL Mater. 6 (5) (2018) 058302, doi:10.1063/1.5021044.

[53] J.L. Braun, D.H. Olson, J.T. Gaskins, P.E. Hopkins, A steady-state thermoreflectance method to measure thermal conductivity, Rev. Sci. Instrum. 90 (2) (2019) 024905, doi:10.1063/1.5056182.

[54] M.S.B. Hoque, Y.R. Koh, J.L. Braun, A. Mamun, Z. Liu, K. Huynh, M.E. Liao, K. Hussain, Z. Cheng, E.R. Hoglund, et al., High in-plane thermal conductivity of aluminum nitride thin films, ACS Nano (2021), doi:10.1021/acsnano.0c09915.

[55] M.S.B. Hoque, Y.R. Koh, K. Aryana, E.R. Hoglund, J.L. Braun, D.H. Olson, J.T. Gaskins, H. Ahmad, M.M.M. Elahi, J.K. Hite, Z.C. Leseman, W.A. Doolittle, P.E. Hopkins, Thermal conductivity measurements of sub-surface buried substrates by steady-state thermoreflectance, Rev. Sci. Instrum. 92 (2021) 064906, doi:10.1063/5.0049531.

[56] Y.R. Koh, M.S.B. Hoque, H. Ahmad, D.H. Olson, Z. Liu, J. Shi, Y. Wang, K. Huynh, E.R. Hoglund, K. Aryana, et al., High thermal conductivity and thermal boundary conductance of homoepitaxially grown gallium nitride (GaN) thin films, Phys. Rev. Mater. 5 (10) (2021) 104604, doi:10.1103/PhysRevMaterials.5.104604.

[57] M. Pletea, W. Brückner, H. Wendrock, R. Kaltofen, Stress evolution during and after sputter deposition of cu thin films onto Si (100) substrates under various sputtering pressures, J. Appl. Phys. 97 (5) (2005) 054908, doi:10.1063/1.1858062.

[58] A. Navid, E. Chason, A. Hodge, Evaluation of stress during and after sputter deposition of Cu and Ta films, Surf. Coat. Technol. 205 (7) (2010) 2355–2361, doi:10.1016/j.surfcoat.2010.09.020.

[59] T. Kaub, Z. Rao, E. Chason, G.B. Thompson, The influence of deposition parameters on the stress evolution of sputter deposited copper, Surf. Coat. Technol. 357 (2019) 939–946.

[60] P. Gouy-Pailler, Y. Pauleau, Tungsten and tungsten–carbon thin films deposited by magnetron sputtering, J. Vac. Sci. Technol. A 11 (1) (1993) 96–102, doi:10.1116/1.578725.

[61] Y. Shen, Y. Mai, Q. Zhang, D. McKenzie, W. McFall, W. McBride, Residual stress, microstructure, and structure of tungsten thin films deposited by magnetron sputtering, J. Appl. Phys. 87 (1) (2000) 177–187, doi:10.1063/1.371841.

[62] L. Romano-Brandt, E. Salvati, E. Le Bourhis, T. Moxham, I.P. Dolbnya, A.M. Korsunsky, Nano-scale residual stress depth profiling in Cu/W nano-multilayers as a function of magnetron sputtering pressure, Surf. Coat. Technol. 381 (2020) 125142, doi:10.1016/j.surfcoat.2019.125142.

[63] N. Kaiser, Review of the fundamentals of thin-film growth, Appl. Opt. 41 (16) (2002) 3053–3060.

[64] J. Floro, S. Hearne, J. Hunter, P. Kotula, E. Chason, S. Seel, C. Thompson, The dynamic competition between stress generation and relaxation mechanisms during coalescence of Volmer–Weber thin films, J. Appl. Phys. 89 (9) (2001) 4886–4897.

[65] E. Chason, B. Sheldon, L. Freund, J. Floro, S. Hearne, Origin of compressive residual stress in polycrystalline thin films, Phys. Rev. Lett. 88 (15) (2002) 156103, doi:10.1103/PhysRevLett.88.156103.

[66] F. Spaepen, Interfaces and stresses in thin films, Acta Mater. 48 (1) (2000) 31–42, doi:10.1016/S1359-6454(99)00286-4.
[67] I.C. Noyan, J.B. Cohen, Residual Stress: Measurement by Diffraction and Interpretation, Springer, 2013.
[68] D. Ariosa, C. Cancellieri, V. Araullo-Peters, M. Chiodi, E. Klyatskina, J. Janczak-Rusch, L.P. Jeurgens, Modeling of interface and internal disorder applied to XRD analysis of Ag-based nano-multilayers, ACS Appl. Mater. Interfaces 10 (24) (2018) 20938–20949, doi:10.1021/acsami.8b02653.
[69] Inorganic Crystal Structure Database | FIZ Karlsruhe, https://www.fiz-karlsruhe.de/de/produkte-und-dienstleistungen/inorganic-crystal-structure-database-icsd. Coll. Code: 15985.
[70] Inorganic Crystal Structure Database | FIZ Karlsruhe. https://www.fiz-karlsruhe.de/de/produkte-und-dienstleistungen/inorganic-crystal-structure-database-icsd. Coll. Code: 43667.
[71] L.P. Jeurgens, Z. Wang, E.J. Mittemeijer, Thermodynamics of reactions and phase transformations at interfaces and surfaces, Int. J. Mater. Res. 100 (10) (2009) 1281–1307, doi:10.3139/146.110204.
[72] A. Druzhinin, C. Cancellieri, L. Jeurgens, B. Straumal, The effect of interface stress on the grain boundary grooving in nanomaterials: application to the thermal degradation of Cu/W nano-multilayers, Scr. Mater. 199 (2021) 113866, doi:10.1016/j.scriptamat.2021.113866.
[73] L. Romano Brandt, E. Salvati, D. Wermeille, C. Papadaki, E. Le Bourhis, A.M. Korsunsky, Stress-assisted thermal diffusion barrier breakdown in ion beam deposited Cu/W nano-multilayers on Si substrate observed by in situ GISAXS and transmission EDX, ACS Appl. Mater. Interfaces 13 (5) (2021) 6795–6804, doi:10.1021/acsami.0c19173.
[74] F. Genin, W. Mullins, P. Wynblatt, The effect of stress on grain boundary grooving, Acta Metall. Mater. 41 (12) (1993) 3541–3547, doi:10.1016/0956-7151(93)90234-J.
[75] A. Druzhinin, G. Lorenzin, D. Ariosa, S. Siol, B. Straumal, J. Janczak-Rusch, L. Jeurgens, C. Cancellieri, The effect of the graded bilayer design on the strain depth profiles and microstructure of Cu/W nano-multilayers, Mater. Des. 209 (2021) 110002, doi:10.1016/j.matdes.2021.110002.
[76] A.V. Druzhinin, B. Rheingans, S. Siol, B.B. Straumal, J. Janczak-Rusch, L.P. Jeurgens, C. Cancellieri, Effect of internal stress on short-circuit diffusion in thin films and nanolaminates: application to Cu/W nano-multilayers, Appl. Surf. Sci. 508 (2020) 145254, doi:10.1016/j.apsusc.2020.145254.
[77] M. Chiodi, C. Cancellieri, F. Moszner, M. Andrzejczuk, J. Janczak-Rusch, L.P.H. Jeurgens, Massive Ag migration through metal/ceramic nano-multilayers: an interplay between temperature, stress-relaxation and oxygen-enhanced mass transport, J. Mater. Chem. C 4 (2016) 4927–4938, doi:10.1039/C6TC01098A.
[78] J. Salter, P. Charsley, The effect of grain size on the lattice thermal conductivity of copper aluminium alloys, Phys. Status Solidi (b) 21 (1) (1967) 357–368, doi:10.3139/146.110204.
[79] B. Feng, Z. Li, X. Zhang, Effect of grain-boundary scattering on the thermal conductivity of nanocrystalline metallic films, J. Phys. D 42 (5) (2009) 055311, doi:10.1088/0022-3727/42/5/055311.
[80] S. Akhanda, R. Matin, M. Bashar, M. Sultana, A. Kowsar, M. Rahaman, Z. Mahmood, Effect of annealing atmosphere on structural and optical properties of CZTS thin films prepared by spin-coating, Bangladesh J. Sci. Ind. Res. 53 (1) (2018) 13–20, doi:10.3329/bjsir.v53i1.35905.
[81] S. Mason, D. Wesenberg, A. Hojem, M. Manno, C. Leighton, B. Zink, Violation of the Wiedemann–Franz law through reduction of thermal conductivity in gold thin films, Phys. Rev. Mater. 4 (6) (2020) 065003, doi:10.1103/PhysRevMaterials.4.065003.
[82] E. Alleno, L. Chen, C. Chubilleau, B. Lenoir, O. Rouleau, M. Trichet, B. Villeroy, Thermal conductivity reduction in CoSb 3–CeO 2 nanocomposites, J. Electron. Mater. 39 (9) (2010) 1966–1970, doi:10.1007/s11664-009-1043-5.
[83] T. Shuvra Basu, R. Yang, S. Joottu Thiagarajan, S. Ghosh, S. Gierlotka, M. Ray, Remarkable thermal conductivity reduction in metal-semiconductor nanocomposites, Appl. Phys. Lett. 103 (8) (2013) 083115, doi:10.1063/1.4819454.
[84] Z.-Y. Li, J.-F. Li, W.-Y. Zhao, Q. Tan, T.-R. Wei, C.-F. Wu, Z.-B. Xing, PbTe-based thermoelectric nanocomposites with reduced thermal conductivity by sic nanodispersion, Appl. Phys. Lett. 104 (11) (2014) 113905, doi:10.1063/1.4869220.
[85] S. Akhanda, R. Matin, M. Bashar, A. Kowsar, M. Rahaman, Z. Mahmood, Experimental study on structural optical and electrical properties of chemical bath deposited CdZnS thin films, J Fundam. Renew. Energy Appl. 7 (2017) 222.
[86] Giacomo Lorenzin, et al., Tensile and compressive stresses in Cu/W multilayers: correlation with microstructure, thermal stability, and thermal conductivity, 2022. http://doi.org/10.5281/zenodo.7039958.